Revealing of the Activation Pathway and Cathode Electrolyte Interphase Evolution of Li-rich $0.5Li_2MnO_3 \cdot 0.5LiNi_{0.3}Co_{0.3}Mn_{0.4}O_2$ Cathode by In-Situ Electrochemical Quartz Crystal Microbalance

Zu-Wei Yin,[†,∥] Xin-Xing Peng,[‡,∥] Jun-Tao Li,*[,†] Chong-Heng Shen,[‡] Ya-Ping Deng,[†] Zhen-Guo Wu,[†,§] Tao Zhang,[†] Qiu-Bo Zhang,[#,∥] Yu-Xue Mo,[†] Kai Wang,[†,§] Ling Huang,[‡] Haimei Zheng,*[,∥,⊥] and Shi-Gang Sun*[,†,‡]

[†]College of Energy and [‡]State Key Lab of Physical Chemistry of Solid Surface, College of Chemistry and Chemical Engineering, Xiamen University, Xiamen 361005, China

[∥]Materials Sciences Division, Lawrence Berkeley National Laboratory, Berkeley, California 94720, United States

[⊥]Department of Materials Science and Engineering, University of California, Berkeley, California 94720, United States

[§]School of Chemical Engineering, Sichuan University, Chengdu 610065, China

[#]SEU-FEI Nano-Pico Center, Key Laboratory of MEMS of Ministry of Education, School of Electronic Science and Engineering, Southeast University, Nanjing 210018, China

Abstract

The first-cycle behavior of layered Li-rich oxides, including Li_2MnO_3 activation and cathode electrolyte interphase (CEI) formation, significantly influences their electrochemical performance. However, the Li_2MnO_3 activation pathway and the CEI formation process are still controversial. Here, the first-cycle properties of $xLi_2MnO_3 \cdot (1-x)\ LiNi_{0.3}Co_{0.3}Mn_{0.4}O_2$ (x = 0, 0.5, 1) cathode materials were studied with an in-situ electrochemical quartz crystal microbalance (EQCM). The results demonstrate that a synergistic effect between layered Li_2MnO_3 and $LiNi_{0.3}Co_{0.3}Mn_{0.4}O_2$ structures can significantly affect the activation pathway of $Li_{1.2}Ni_{0.12}Co_{0.12}Mn_{0.56}O_2$, leading to an extra-high capacity. It is demonstrated that Li_2MnO_3 activation in Li-rich materials is dominated by electrochemical decomposition (oxygen redox), which is different from the activation process of pure Li_2MnO_3 governed by chemical decomposition (Li_2O evolution). CEI evolution is closely related to Li^+ extraction/insertion. The valence state variation of the metal ions (Ni, Co, Mn) in Li-rich material can promote CEI formation. This study is of significance for understanding and designing Li-rich cathode-based batteries.

Key words: Li-rich materials, Li_2MnO_3 activation, oxygen redox, CEI evolution, in-situ EQCM

1. Introduction

Continuing interest in sustainable use of Li-ion batteries (LIBs) for electrical transportation is driving further developments in cathode materials. Layered Li-rich oxide cathode materials exhibit high specific capacity of more than 250 mAh g^{-1} and thus are considered as potential candidates for the next-generation LIBs.[1-2] Nevertheless, commercial applications of Li-rich cathode materials are hindered by three main drawbacks. First, a large irreversible capacity loss happens in the first charge-discharge process. Second, their cyclability and rate capability are not sufficient. Third, significant voltage decay occurs during cycling.[3-5] All these issues are highly related to the first-cycle charge-discharge processes. Therefore, a better understanding and further controlling of the first-cycle processes of the Li-rich oxide cathode will be beneficial to improve its electrochemical properties.

Li_2MnO_3 activation and cathode electrolyte interphases (CEI) formation/dissolution are two key reactions of Li-rich oxides in the first cycle. Many previous studies have been done to understand the activation process of Li_2MnO_3 and CEI evolution. However, there is no consensus on the Li_2MnO_3 activation process.[6-11] For example, it was claimed that O^{2-} was oxidized to an O_2^{2-} species or O_2^{2-}-like localized electron holes on oxygen ("oxygen redox") during Li_2MO_3 (M =Ru, Sn, Mn) activation .[6-9] In contrast, other studies show very different Li_2O evolution processes.[10-11] So far, most results were achieved using ex-situ electron paramagnetic resonance (EPR), X-ray photoelectron spectroscopy (XPS),[6] resonant inelastic X-ray scattering (RIXS),[7] in-situ Raman,[9-10] and wavelength dispersive spectroscopy (WDS)[11]. However, an important limitation of these experimental studies is that only surface information can be obtained.[6-7,9-11]

Electrochemical quartz crystal microbalance (EQCM) is able to detect in real time the mass change of a bulk electrode with high sensitivity during electrochemical processes.[12-14] For example, EQCM was used as a gravimetric probe to detect concentration and compositional changes of microporous activated carbons.[12] EQCM was also adapted to analyze formation of electrode/electrolyte interphase on graphite and Sn thin film electrodes.[15,23] CEI formation on the Li-rich $0.5Li_2MnO_3 \cdot 0.5LiMn_{0.375}Ni_{0.375}Co_{0.25}O_2$ surface was also studied by EQCM, but the relationship between reaction in Li-rich electrodes and CEI formation was not clarified.[25]

There are two different activation pathways that can lead to mass loss of Li-rich cathode materials, namely electrochemical decomposition (oxygen redox)[6-9] and chemical decomposition (Li_2O evolution)[10-11]. The mass loss can be used as a criterion to differentiate the decomposition processes because electrochemical decomposition leads to Li^+ de-intercalation from electrode while no Li^+ de-intercalation occurs during chemical decomposition. In this study, we applied in-situ EQCM to investigate the first-cycle charge-discharge processes of $Li_{1.2}Ni_{0.12}Co_{0.12}Mn_{0.56}O_2$ ($0.5Li_2MnO_3 \bullet 0.5LiNi_{0.3}Co_{0.3}Mn_{0.4}O_2$), Li_2MnO_3 and $LiNi_{0.3}Co_{0.3}Mn_{0.4}O_2$ electrode materials. We found that the activation pathway of Li_2MnO_3 in $Li_{1.2}Ni_{0.12}Co_{0.12}Mn_{0.56}O_2$ is influenced by synergistic effects between Li_2MnO_3 and $LiNi_{0.3}Co_{0.3}Mn_{0.4}O_2$. Our results show that the Li_2MnO_3 activation in Li-rich material is dominated by electrochemical decomposition (oxygen redox), as opposed to activation of pure Li_2MnO_3, which is governed by chemical decomposition (Li_2O evolution). CEI formation is evidently affected by changes in the valence states of metal ions in Li-rich material. Our study has deepened the understanding of the first-cycle behavior of Li-rich materials, which will be helpful for designing Li-rich cathode-based batteries.

2. Experimental

2.1. Materials Preparation and Characterization

A modified Pechini method was adopted to prepare Li_2MnO_3, $LiNi_{0.3}Co_{0.3}Mn_{0.4}O_2$ and $Li_{1.2}Ni_{0.12}Co_{0.12}Mn_{0.56}O_2$ materials, as reported in our previous study.[16] Citric acid, dissolved in ethylene glycol in a 1:4 molar ratio, was used as chelating agent. Then a metal ion solution containing a stoichiometric amount of $Li(CH_3COO)\cdot H_2O$ (an excess of 5% in molar ratio), $Ni(CH_3COO)_2\cdot 4H_2O$, $Mn(CH_3COO)_2\cdot 4H_2O$ and $Co(CH_3COO)_2\cdot 4H_2O$ was added dropwise. A clear solution was obtained after heating at 90 ℃ while stirring for 1 h. The resulting solution was further heated at 140 ℃ to esterify and evaporate the excess water. The residue was vacuum dried in an oven at 180 ℃ for 12 h for thermal polymerization to yield an organic polymer foam. The obtained precursor was pre-heated at 450 ^oC for 6 h, and then calcined at 700 ^oC for 24 h.

The microstructure and crystal structure were characterized by scanning electron microscope (SEM, Hitachi S-4800) and powder X-ray diffraction (XRD, Philips X'Pert Pro), respectively. XRD measurements were run over the 2θ range of 15-90 º. The scan rate was 1 $^o min^{-1}$. XRD refinement was conducted by Rietveld method using Topas program (Bruker, Topas 4.2).

2.2. EQCM Measurements

(1) Preparation of materials modified quartz crystal electrode

Slurry composed of 80 wt. % cathode materials, 10 wt. % acetylene black and 10 wt. % PVDF in N-methylpyrrolidone was prepared and dripped on the Au-coated AT-cut 7.995 MHz 1 inch diameter quartz crystal surface. Prior to use, the Au-coated crystal was rinsed with ethanol and

acetone for 10 min each, respectively. The loaded active material was controlled at 4.5±0.5 μg. Under this mass load, the quartz crystal can maintain a resonance oscillation ($\Delta f/f_0 < 2\%$. Δf is the mass change of the load, and f_0 is resonance frequency of Au crystal).[17,23] The mass of each material was obtained from the difference between the resonance frequency of the Au-coated crystal with and without active material. The geometric area of the Au electrode was 0.196 cm^2. The prepared quartz crystal was dried at 80 ℃ for 12 h in vacuum. After cooling down, it was fixed on the crystal holder and used as the working electrode. Fig S1a and b shows an optical micrograph of a $Li_{1.2}Ni_{0.12}Co_{0.12}Mn_{0.56}O_2$ slurry-coated quartz crystal after drying at 80 ℃ for 12 h in vacuum and an optical micrograph of the $Li_{1.2}Ni_{0.12}Co_{0.12}Mn_{0.56}O_2$ slurry surface. The loaded material is distributed uniformly in the center of Au crystal.

(2) Details of measurements

EQCM measurements were conducted using a three-electrode system at 25 ℃. Fig 1 shows a schematic diagram of the EQCM setup. Both the reference and the counter electrode are lithium strips. The electrochemical cell assembly was operated in an argon-filled glove box at room temperature. 1 M $LiPF_6$ (LP) dissolved in ethylene carbonate/dimethyl carbonate (EC: DMC = 1:1 v/v) was used as the electrolyte. For each EQCM test, the volume of electrolyte was 0.8 mL. CV-EQCM tests were conducted by a CHI440C EQCM workstation (CH Instruments) and its accessories. For this equipment, a 1 Hz frequency increase means a 1.34 ng weight decrease. Before the CV-EQCM tests, the three-electrode system was kept standing for 6 h to reach steady state. CV curves were generated between 2.0 V to 4.8 V with a scanning rate of 0.2 mV s^{-1}. The mass change of the working electrodes was recorded by the EQCM during the CV measurements.

When $\Delta f/f_0 < 2\%$, the *mpe* (mass accumulated per mole of electron transferred) values were estimated according to the Sauerbrey equation (eq 1) and Faraday's law (eq 2),[17,23]

$$\Delta \boldsymbol{m} = -\frac{\boldsymbol{A}(\boldsymbol{\mu_q}\boldsymbol{\rho_q})^{\mathbf{0.5}}\Delta \boldsymbol{f}}{\mathbf{2}\boldsymbol{f_0^2}} = -\boldsymbol{C_f}\cdot\Delta \boldsymbol{f} \quad (1)$$

$$\boldsymbol{mpe} = \boldsymbol{nF}\cdot\frac{\Delta \boldsymbol{m}}{\boldsymbol{Q}} = -\boldsymbol{nC_fF}\frac{\Delta \boldsymbol{f}}{\boldsymbol{Q}} \quad (2)$$

where Δm is the mass change, $\Delta \boldsymbol{f}$ is the change in resonance frequency, f_0 is the fundamental resonance frequency (7.995 MHz), A is the surface area of the electrode (0.196 cm^2), $\boldsymbol{\mu_q}$ is the shear modulus of quartz ($2.947*10^{11}$ $g{\cdot}cm^{-1}{\cdot}s^{-2}$), $\boldsymbol{\rho_q}$ is the density of quartz (2.684 $g\ cm^{-3}$), $\boldsymbol{C_f}$ is the sensitivity factor for this setup (1.34 $ng{\cdot}Hz^{-1}$), Q is the charge passed through the electrode in Coulombs, F is the Faraday constant (96485 $C\ mol^{-1}$), and n is the valence number of the ion.

However, the Sauerbrey equation always needs a correction related to the electrode/electrolyte interface. Another factor that affects the frequency shift is the change of density ($\boldsymbol{\rho_L}$) and viscosity ($\boldsymbol{\eta_L}$) of the electrolyte in contact with the quartz crystal electrode,[16,26] as follows

$$\Delta \boldsymbol{f_{\eta\rho}} = -\boldsymbol{f_0^{\frac{3}{2}}}\left[\frac{\Delta(\boldsymbol{\eta_L}\boldsymbol{\rho_L})}{\pi \boldsymbol{\mu_q}\boldsymbol{\rho_q}}\right]^{\frac{1}{2}} \quad (3)$$

The observed frequency change Δf is the sum of the frequency change associated with mass loss/gain ($\Delta \boldsymbol{f_m}$) and the change in ($\boldsymbol{\eta_L}\boldsymbol{\rho_L}$) during the electrochemical process:

$$\Delta f = \Delta f_m + \Delta f_{\eta\rho} \quad (4)$$

$\Delta(\boldsymbol{\eta_L}\boldsymbol{\rho_L})$ can be estimated from the change in the resistance of the quartz crystal ($\Delta \boldsymbol{R}$),

$$\Delta \boldsymbol{R} = [\mathbf{2}\pi \boldsymbol{f_0}\Delta(\boldsymbol{\eta_L}\boldsymbol{\rho_L})]^{\mathbf{1/2}}\boldsymbol{A}/\boldsymbol{k^2} = -[\pi(\mathbf{2}\,\boldsymbol{\mu_q}\boldsymbol{\rho_q})^{\frac{1}{2}}\boldsymbol{A}/(\boldsymbol{k^2 f_0})]\,\Delta \boldsymbol{f_{\eta\rho}} \quad (5)$$

where k is an electromechanical factor. From eq 5, we see that $\Delta \boldsymbol{f_{\eta\rho}}$ has a negative linear correlation with $\Delta \boldsymbol{R}$. However, due to the inhomogeneous concentration of electrolyte near

electrode during charge-discharge process (including density and viscosity, $\boldsymbol{\eta_L \rho_L}$), and the $\boldsymbol{\Delta R}$ is also affected by roughness of electrode, which changes when strong deposition reaction occurs, such as electrolyte decomposition at $<$ 2.6 V region.[26] It is difficult to make an accurate quantitatively relationship between $\boldsymbol{\Delta R}$ and $\boldsymbol{\Delta f_{\eta\rho}}$. In this work, we used $\boldsymbol{\Delta R}$ to do a qualitative correction of obtained $\boldsymbol{\Delta f}$ from tests. An increase of $\boldsymbol{\Delta R}$ means a decrease of $\boldsymbol{\Delta f_{\eta\rho}}$.

2.3. Electrochemical Measurements

CR2025-type coin cells were used to measure the electrochemical performance. A mixture of the synthesized material, polyvinylidenediuoride (PVDF) binder and acetylene black at a weight ratio of 8: 1: 1 soaked in N-methyl-2-pyrrolidone (NMP) solvent was coated on a 16 mm diameter Al foil current collector to prepare the electrode. The electrodes were dried at 100 ℃ for 12 h in vacuum before each test. The weight of active material in each electrode was kept at 1.25±0.1 mg cm^{-2}. An argon-filled glove box was used to assemble the CR2025-type coin cells. Lithium foils and Celgard 2400 film were used as counter electrode and separator, respectively. 1 M $LiPF_6$/EC/DMC (EC: DMC = 1:1 v/v, H_2O concentration $<$ 5 ppm) was used as the electrolyte. A Land-V34 battery tester (Wuhan, China) was used for galvanostatic control of the cells, which were kept at 30 ^oC. The current density of 1 C equals to 200 mA g^{-1}. Capacities were calculated based on the weight of active material. A ChI660E work station was used to do cyclic voltammetry test. All the materials were tested between 2.0 and 4.8 V (*vs*. Li/Li^+) at a scan rate of 0.2 mV s^{-1}.

Electrochemical impedance spectroscopy (EIS) was performed on a VSP multichannel potentiostatic-galvanostatic system (VERSASTATV3, USA). The electrode potential was increased

stepwise from open circuit voltage (OCP) to 4.8 V and then decreased to 2.0 V with 0.1-0.2 V potentiostatic steps. Before EIS tests at each potential, the voltage was kept constant for 20 mins. The impedance spectra were recorded by applying an AC voltage of 5 mV in the frequency range from 1 MHz to 5 mHz.

3. Results and Discussion

3.1 Microstructure, crystal structure and electrochemical performance

Fig 2a-c shows SEM images of Li_2MnO_3, $LiNi_{0.3}Co_{0.3}Mn_{0.4}O_2$ and $Li_{1.2}Ni_{0.12}Co_{0.12}Mn_{0.56}O_2$. All the samples have similar microstructures, but the particle sizes are different. The Li_2MnO_3 and $Li_{1.2}Ni_{0.12}Co_{0.12}Mn_{0.56}O_2$ particles were between 100 and 200 nm, while those of $LiNi_{0.3}Co_{0.3}Mn_{0.4}O_2$ ranged from 200 and 300 nm. XRD profiles are displayed in Figure 2d. All of these three samples have distinct features indicating a layered structure. For $Li_{1.2}Ni_{0.12}Co_{0.12}Mn_{0.56}O_2$ and $LiNi_{0.3}Co_{0.3}Mn_{0.4}O_2$, the strong peaks at 18.7 ° and 44.6 ° can be indexed to (003) and (104) planes of the α-$NaFeO_2$ parent hexagonal structure ($R\bar{3}m$ symmetry). Li_2MnO_3 exhibits monoclinic structure with strong peaks at 18.6 ° and 44.7 °, which correspond to (001) and (131) planes of space group *C2/m*.[9] Both $Li_{1.2}Ni_{0.12}Co_{0.12}Mn_{0.56}O_2$ and Li_2MnO_3 have a broad superlattice (110) peak at 20-25 °, which indicates cation ordering in the transition-metal layer and stacking faults formed during materials preparing process.[9] Fig S2 shows the refinement XRD patterns of $Li_{1.2}Ni_{0.12}Co_{0.12}Mn_{0.56}O_2$. The calculated ratio of Li_2MnO_3 and $LiMO_2$ (M = Ni, Co, Mn) is 48.9:51.1, which is very close to 50:50. Considering the calculation error, it is acceptable to denote Li-rich material as $0.5Li_2MnO_3 \bullet 0.5LiNi_{0.3}Co_{0.3}Mn_{0.4}O_2$. More detailed structure information of $Li_{1.2}Ni_{0.12}Co_{0.12}Mn_{0.56}O_2$ can be seen in our previous study.[16]

Fig 2e displays the initial charge-discharge profiles of Li_2MnO_3, $LiNi_{0.3}Co_{0.3}Mn_{0.4}O_2$ and $Li_{1.2}Ni_{0.12}Co_{0.12}Mn_{0.56}O_2$ at 0.1 C. For Li_2MnO_3, only a voltage plateau above 4.4 V is observed during charge.[10] Instead of a very stable plateau at ~4.5 V, the inclined plateau is attributed to the low conductivity of pure Li_2MnO_3.[10,28] During discharge, the voltage declines rapidly, showing a capacity of only 126.8 mAh g^{-1}. The irreversible capacity ratio (ICR), defined as irreversible capacity divided by charge capacity, was 48.85%. During charge, $LiNi_{0.3}Co_{0.3}Mn_{0.4}O_2$ has a voltage plateau above 3.7 V, corresponding to Ni^{2+}/Ni^{4+} and Co^{3+}/Co^{4+} redox couples. It has a discharge capacity of 178.7 mAh g^{-1} and an 18.92% ICR. $Li_{1.2}Ni_{0.12}Co_{0.12}Mn_{0.56}O_2$ has a capacity of 120 mAh g^{-1} during the initial charge process, which is associated with the Ni^{2+}/Ni^{4+} and $Co^{3+}/Co^{3.6+}$ redox couples.[9,17] The plateau above 4.4 V corresponding to Li_2MnO_3 activation is observed and provides an additional capacity of 200 mAh g^{-1}. Upon discharging, $Li_{1.2}Ni_{0.12}Co_{0.12}Mn_{0.56}O_2$ exhibits a sloping voltage curve and has a capacity of 244.7 mAh g^{-1} with 22.56% ICR. The discharge capacity of $Li_{1.2}Ni_{0.12}Co_{0.12}Mn_{0.56}O_2$ is much higher than the average of Li_2MnO_3 and $LiNi_{0.3}Co_{0.3}Mn_{0.4}O_2$, indicating a synergistic effect between Li_2MnO_3 and the layered structure in Li-rich oxide material. Lim et al. has proved that layered $LiNi_{1/3}Co_{1/3}Mn_{1/3}O_2$ benefits from the structural stability of Li_2MnO_3.[18] However, the explanation for why extra capacity results from the introduction of Li_2MnO_3 into layered $LiNi_{0.3}Co_{0.3}Mn_{0.4}O_2$ is unclear.

The CV profiles (for the first cycle) of Li_2MnO_3, $LiNi_{0.3}Co_{0.3}Mn_{0.4}O_2$ and $Li_{1.2}Ni_{0.12}Co_{0.12}Mn_{0.56}O_2$ are shown in Fig 2f. For Li_2MnO_3, no anodic peak emerges until ~ 4.4 V. The current peak between 4.4 and 4.8 V is attributed to Li_2MnO_3 activation and simultaneous lithium extraction. A small reductive current peak can be observed below 3.6 V

corresponding to Mn^{4+}/Mn^{3+} reduction. The anodic and cathodic current densities of Li_2MnO_3 are distinctly smaller than those of $LiNi_{0.3}Co_{0.3}Mn_{0.4}O_2$ and $Li_{1.2}Ni_{0.12}Co_{0.12}Mn_{0.56}O_2$. For $LiNi_{0.3}Co_{0.3}Mn_{0.4}O_2$, the first peak between 3.65 V and 4.3 V during charge corresponds to Ni^{2+}/ Ni^{4+} and $Co^{3+}/Co^{3.6+}$ redox couples. The second smaller peak at ~4.5 V is due to the $Co^{3.6+}/Co^{4+}$ redox couple.[17] A reduction peak centered at ~3.7 V is observed, which is attributed to Ni^{4+}/Ni^{2+} and Co^{4+}/Co^{3+} redox couples. Below 3.0 V, no peak is observed, which indicates no Mn^{3+} formation. The CV profile of $Li_{1.2}Ni_{0.12}Co_{0.12}Mn_{0.56}O_2$ shows anodic peaks between 3.65 V and 4.4 V for the Ni^{2+}/Ni^{4+} and $Co^{3+}/Co^{3.6+}$ redox couples.[17] The subsequent oxidation peak from 4.4 to 4.8 V is due to Li_2MnO_3 activation and lithium extraction, which is similar to that of Li_2MnO_3. During reduction, the Ni^{4+}/ Ni^{2+} and Co^{4+}/Co^{3+} redox peaks at ~3.8 V resembles $LiNi_{0.3}Co_{0.3}Mn_{0.4}O_2$.[5]

3.2 First-cycle interfacial properties

Fig 3a displays the first cycle CV curve and the simultaneous EQCM response of $Li_{1.2}Ni_{0.12}Co_{0.12}Mn_{0.56}O_2$. The corresponding $\Delta f - \Delta Q$ (charge) plots are shown in Fig 3b and c. To help interpret these observations, analogous data pure $LiPF_6$/EC+DMC, without loaded materials are depicted in Fig S3.

The diagrams of ΔR versus E (electrode potential) of pure $LiPF_6$/EC+DMC electrolyte, $Li_{1.2}Ni_{0.12}Co_{0.12}Mn_{0.56}O_2$, $LiNi_{0.3}Co_{0.3}Mn_{0.4}O_2$ and Li_2MnO_3 during first CV cycle are shown in Fig S4.

In many regions, the variation of ΔR is negligible (~0), so the Sauerbrey equation is still valid, which is similar to Tsai's and Wu's reports.[14,20] For example, in the 4.4-4.65 V region

during the first anodic scanning of $Li_{1.2}Ni_{0.12}Co_{0.12}Mn_{0.56}O_2$, Li_2MnO_3 activation occurs and the variation of ΔR is near to zero. In many other regions, the variation of ΔR is not so obvious, so the mass loss/gain is the main process affecting the shift in frequency ($\Delta \boldsymbol{f}$). In this study, we first calculated the mass changes and *mpe* values by the Sauerbrey equation, and then we analyzed and adjusted the *mpe* values with ΔR. The obtained values of these parameters are listed in Table 1.

Fig 2e and Fig 3a illustrate that the capacity, current and $\Delta \boldsymbol{f}$ are all very small between open circuit potential (OCP) and 3.7 V during the first charge. Changes in this region are attributed mainly to absorption/desorption of electrolyte molecules or ions.[27] In the first charge, ΔR is almost zero when the potential is below 4.65 V, which suggests the Sauerbrey equation is valid in this region. It is observed that the measured *mpe* is close to 7 g mol^{-1} (which is the atomic weight of Li) in the 4.2-4.4 V region, which indicates delithiation of Li^+ along with Ni^{2+}/ Ni^{4+} and Co^{3+}/ $Co^{3.6+}$ oxidation reactions.[19] However, the *mpe* values in 3.7-4.2 V and 4.4-4.65 V are higher than 7 g mol^{-1}, indicating additional processes. For analyzing the formation/dissolution of CEI, ΔR_{CEI}-E plots at different potential during the first charge are displayed as a red line in Fig 3d. The corresponding Nyquist plots are shown in Fig S5a-d. The equivalent circuit, shown as an insert in Fig3d, was applied to analyze the EIS data. In this equivalent circuit, R_S represents the internal resistance of the battery, R_{CEI} and C_{CEI} represent the resistance and capacitance of the CEI film, while R_{ct} and C_{dl} represent the charge-transfer resistance and double-layer capacitance. W is the Warburg impedance related to Li^+ diffusion.[21] The fitted impedance parameters are listed in Table S1. There is always native surface film on most cathode surfaces (Li_2CO_3 on lithium transition metal

oxides).[22] This is the source of R_{CEI} in the initial state. It can be seen that the R_{CEI} decreases with the potential increases in 3.7-4.2 V region, which indicates the dissolution of CEI layer. There is always HF in electrolyte. Native Li_2CO_3 can react with HF and lead to dissolution.[24] Electrochemical decomposition of Li_2CO_3 was also reported by previous study.[27] So the Li_2CO_3 degradation is a possible pathway of CEI dissolution, which can make the measured *mpe* value higher. This is consistent with the high *mpe* value in 3.7-4.2 V region. In the 4.4-4.65 V region, R_{CEI} increases slightly, indicating new CEI film produced. So the mass change is attributed to the irreversible decomposition of the Li_2MnO_3 component in $Li_{1.2}Ni_{0.12}Co_{0.12}Mn_{0.56}O_2$ and to CEI formation. Fig S3 further confirms the above analysis. The decreased Δf during charge indicates no gold base dissolution (increased Δf), which means gold is stable in $LiPF_6$/EC+DMC electrolyte. The Δf vary is originated from electrolyte reactions. For pure $LiPF_6$/EC+DMC electrolyte, the absorption/desorption process of electrolyte molecules/ions occurs in the OCP-4 V region. In the 4-4.65 V region, it can be observed from CV curve that electrolyte begins to oxidize. Frequency decrease and negligible ΔR can also be seen, corresponding to a mass increase and indicating the CEI layer derived from electrolyte formed. CEI formation can reduce the calculated *mpe* value. In 3.7-4.2 V region of $Li_{1.2}Ni_{0.12}Co_{0.12}Mn_{0.56}O_2$, native CEI layer dissolved. But the *mpe* value in the 4-4.2 V region is smaller than that in 3.7-4 V, which is attributed to new CEI film formation derived from electrolyte. Between 4.2 and 4.4 V, the *mpe* value is slightly smaller than 7 g mol^{-1}, which is also attributed to new CEI formation. In the 4.4 V-4.65 V region, the mass change is attributed to the irreversible decomposition of Li_2MnO_3 component in $Li_{1.2}Ni_{0.12}Co_{0.12}Mn_{0.56}O_2$ and to CEI formation.

There have been many studies about the decomposition of Li_2MnO_3, and O_2^{2-} (true species or localized electron holes on oxygen). Li_2O were proved to be formed in different research.[6-10] The specific reactions may follow as eq 6 and eq 7.

$$\boldsymbol{2Li_2MnO_3 \rightarrow 4Li^+ + O_2^{2-} + 2MnO_2 + 2e^-} \quad (6)$$

$$\boldsymbol{Li_2MnO_3 \rightarrow Li_2O + MnO_2} \quad (7)$$

For eq 6, two electrons are transferred and four Li^+ ions are extracted. The *mpe* value of eq 6 is 28/2 =14 g mol^{-1} and Li^+ extraction can lead to mass loss. For eq 7, no electrons are transferred and no species are lost from the material, so the mass change of eq 7 is zero. As can be seen in Table 4, the maximum of mass loss of $Li_{1.2}Ni_{0.12}Co_{0.12}Mn_{0.56}O_2$ in 4.4-4.65 V region is 277.4 ng when eq 6 is the only reaction. However, the real mass loss is 137.5 ng, which is 49.57% of the maximal mass loss originating from Li_2MnO_3 activation. Considering that CEI film formation leads to mass gain, and chemical decomposition according to eq 7 does not affect the mass, electrochemical decomposition according to eq 6 is the main process of Li_2MnO_3 activation for Li-rich oxide $Li_{1.2}Ni_{0.12}Co_{0.12}Mn_{0.56}O_2$.The measured *mpe* value in 4.4-4.65 V region is 12.85 g mol^{-1}, which is slightly smaller than 14 for eq 6. CEI film formation leads to a mass gain for the electrode, but no electrons transfer of electrode material, and makes the measured *mpe* value smaller, which is consistent with our experiment. In the region above 4.65 V, the ΔR is slightly increased, and a further oxidation reaction of electrolyte occurs because of the high charge voltage.

Fig 3c illustrates the Δf $-\Delta Q$ plot during the first discharge process, and the corresponding mass change and *mpe* values are listed in Table 1. ΔR increases during the first discharge, which leads to a negative shift of frequency. So the actual shift of frequency

caused by the mass gain is smaller than that observed in Fig 2c, and the real *mpe* value is smaller than that listed in Table 1. In the 4.8-4.1 V region, a continuous oxidation reaction of electrolyte occurs. In the region below 2.6 V, a decomposition reaction of electrolyte occurs, which is consistent with the very small capacity in the charge-discharge curve, as demonstrated in Fig 2e. Considering the previous reports and our experimental data (mpe = 53.42, ΔR increase), Li_2CO_3 (mpe =37) is one of the possible product.[10,28] In these two regions, there are no valence state changes for the metal ions in $Li_{1.2}Ni_{0.12}Co_{0.12}Mn_{0.56}O_2$, and the interfacial reactions for $Li_{1.2}Ni_{0.12}Co_{0.12}Mn_{0.56}O_2$ and pure electrolyte are very similar. In the 4.1-2.6 V region, the insertion of Li^+ causes the mass to increase. However, the *mpe* value in the 4.1-2.6 V region is higher than 7 g mol^{-1}, indicating that the insertion of Li^+ maybe not be the only electrochemical process. But considering the shift of frequency caused by ΔR, more proof should be given. The blue line in Fig 3d displays the ΔR_{CEI}-E plot of $Li_{1.2}Ni_{0.12}Co_{0.12}Mn_{0.56}O_2$ at different potentials during the first discharge. The corresponding Nyquist plots are shown in Fig S5e-f, and the fitted impedance parameters are listed in Table S2. It is observed that R_{CEI} increases as the potential decreases in the 4.1-2.6 V region. Considering that the *mpe* value is greater than 7 g mol^{-1}, a new CEI film with lower conductivity has apparently formed in this region. For pure $LiPF_6$/EC+DMC electrolyte, the frequency change is slightly higher in the 4.1-2.6 V region. Considering that an increase in ΔR leads to negative shift of frequency, the measured frequency increase implies CEI dissolution and mass loss. The difference between pure electrolyte and $Li_{1.2}Ni_{0.12}Co_{0.12}Mn_{0.56}O_2$ is attributed to the valence state changes of metal ions in this region,

since the interfacial reactions are very similar when there are no valence state changes of metal ions in the region above 4.1 V and below 2.6 V.

To further clarify the interfacial property of Li-rich $Li_{1.2}Ni_{0.12}Co_{0.12}Mn_{0.56}O_2$ material, the interfacial properties of layered $LiNi_{0.3}Co_{0.3}Mn_{0.4}O_2$ and pure Li_2MnO_3 were also investigated for comparison. As demonstrated in Fig 4a, the CV curve during the first cycle and the simultaneous EQCM response of $LiNi_{0.3}Co_{0.3}Mn_{0.4}O_2$ can be observed. The corresponding $\Delta f - \Delta Q$ plots are shown in Fig 4c and 4e. Table 2 summarizes the mass change and *mpe* values during first cycle. As with $Li_{1.2}Ni_{0.12}Co_{0.12}Mn_{0.56}O_2$, electrolyte absorption/desorption occurs below 3.65 V. The *mpe* value in the 3.65-3.9 V region is near 7 g mol^{-1} and ΔR is insignificant, which indicates delithiation along with Ni^{2+}/ Ni^{4+} and Co^{3+}/ $Co^{3.6+}$ oxidation. In the 3.9-4.4 V region, ΔR increases slightly, while the *mpe* value varies. The large *mpe* values indicate that dissolution of the native CEI layer is the dominated process, as with $Li_{1.2}Ni_{0.12}Co_{0.12}Mn_{0.56}O_2$. When the potential is above 4.4 V, the variation of ΔR is near to zero and the Sauerbrey equation is applicable. In the 4.4-4.53 V region, $Co^{3.6+}$/ Co^{4+} oxidation reactions occur along delithiation.[17] The *mpe* value in the 4.4-4.53 V region is 6.73 g mol^{-1}, which is slightly smaller than 7 g mol^{-1}. This result demonstrates that Li^+ extraction along with $Co^{3.6+}$/ Co^{4+} oxidation are the main processes in this region. Nyquist plots of $LiNi_{0.3}Co_{0.3}Mn_{0.4}O_2$ shown in Fig S6 also illustrate that R_{CEI} is slightly increased, indicating that there is new CEI film formed. When the voltage is higher than 4.65 V, electrolyte oxidation occurs. For the first discharge of $LiNi_{0.3}Co_{0.3}Mn_{0.4}O_2$, it is very similar to that of Li-rich $Li_{1.2}Ni_{0.12}Co_{0.12}Mn_{0.56}O_2$. $\Delta \mathbf{R}$ increases during first discharge, as with $Li_{1.2}Ni_{0.12}Co_{0.12}Mn_{0.56}O_2$. Continuous electrolyte oxidation occurs in the 4.8-4.1 V region and

electrolyte is decomposed when the potential is below 2.6 V. Between 4.1 and 2.6 V, Li^+ insertion is accompanied by metal ion reduction and CEI film formation.

Fig 4b shows the CV curve for the first cycle and the simultaneous EQCM response of Li_2MnO_3. The corresponding $\Delta f - \Delta Q$ (charge) plots are displayed in Fig 4d and f. Table 3 summarizes the *mpe* value during first cycle. For the Li_2MnO_3 electrode, ΔR increases when the voltage is below 3.8 V but hardly varies when the potential is above 3.8 V. There is no obvious electrochemical reaction besides the absorption/desorption of electrolyte molecule/ion when the potential is below 3.8 V. In the 3.8-4.05 V region, the native CEI film dissolves, as with the case of Li-rich material. In the region between 4.05 and 4.4 V, new CEI is produced. In the 4.4-4.65 V region, the Sauerbrey equation is valid and the decomposition of Li_2MnO_3 is the dominant reaction. As displayed in Table 4, the mass of loaded Li_2MnO_3 is 4.777 μg. The maximum extracted Li^+ is 567.589 ng when eq 6 is the only decomposition pathway. However, the real mass loss of Li_2MnO_3 is only 7.959 ng, only 1.4% of the maximal mass loss from Li_2MnO_3 activation and much smaller than 49.57% of Li-rich oxide. The *mpe* value is 1.51 g mol^{-1}, which is distinctly smaller than the 14 g mol^{-1} of eq 6. This result indicates that CEI film formed. Considering that the new CEI film formation can counter some of the mass loss, we conclude that a chemical decomposition of Li_2MnO_3 to Li_2O and MnO_2 is the dominant reaction, as shown in eq 7, which coincides with the electrochemical results in Fig 2f.

However, electrochemical decomposition is the main process of Li_2MnO_3 component in Li-rich oxide $Li_{1.2}Ni_{0.12}Co_{0.12}Mn_{0.56}O_2$. The obviously different routes of Li_2MnO_3 decomposition reactions in the same potential region demonstrates that there is a synergistic effect between Li_2MnO_3 (*C2/m*) and the layered structure ($R\bar{3}m$) in Li-rich oxide material,

which is in accordance with the first charge-discharge profiles in Fig 2e. Pure chemical decomposition does not contribute to capacity. So the different decomposition pathway of Li_2MnO_3 in Li-rich oxides is the reason why Li-rich oxides can provide higher capacity than pure Li_2MnO_3 and $LiNi_{0.3}Co_{0.3}Mn_{0.4}O_2$ materials.

The first discharge of pure Li_2MnO_3 is also very similar to that of Li-rich oxide, where electrolyte oxidation occurs in the 4.8-3.9 V region and electrolyte is decomposed for potentials below 2.6 V. In the region between 3.9 and 2.6 V, Li^+ inserts into the electrode and CEI is formed. But there is some difference. The *mpe* value is much smaller than that of $Li_{1.2}Ni_{0.12}Co_{0.12}Mn_{0.56}O_2$ and $LiNi_{0.3}Co_{0.3}Mn_{0.4}O_2$, indicating that changes in the valence state of Ni^{4+} and Co^{4+} have a bigger effect on CEI formation than those of Mn^{4+} and O_2^{2-}.

Scheme 1a demonstrates the EQCM working principle in this work. The Li^+ insertion/extraction and SEI evolution occurring on the electrodes lead to mass change, which can be measured by the frequency change of crystal quartz. The CV curves can also be recorded, which can be used to calculate the charge evolution during the test. Combining the mass change and charge evolution, we can get the mpe value, which is closely related with different kinds of reactions and important to determine what reactions occur in different potential region, such as Li_2MnO_3 activation in 4.4-4.65 V region during first charge. Scheme 1b illustrates the proposed interfacial reaction mechanism of Li-rich oxides during the first charge, based on the previous results in this article. Solvated electrolyte ions adsorb on the surface of the electrode in the initial period. Subsequently, Li^+ extracts from material. When the potential is below 4.4 V, Ni^{2+} is oxidized to Ni^{4+} to compensate for the Li^+ extraction. Native CEI dissolution takes place at the same time. In the voltage region between 4.4 V and 4.65 V, Li_2MnO_3 activation and new CEI formation occurs. At higher potentials, electrolyte oxidation is the dominant reaction. Detailed reactions in the Li_2MnO_3 activation region of Li-rich oxides and pure Li_2MnO_3 are depicted in scheme 1c. For pure Li_2MnO_3, the activation

process is mainly chemical decomposition to Li_2O and MnO_2. However, for Li-rich oxides, electrochemical decomposition to Li^+, O_2^{2-} and MnO_2 is the dominant pathway. The proposed main interfacial reaction mechanism of Li-rich oxides during first discharge is illustrated in Scheme 1d. Continuous electrolyte oxidation occurs in the high voltage. After the voltage dropping to 4 V, Li^+ insertion accompanied by metal ion and O_2^{2-} reduction subsequently occurs, while CEI forms in the same time. When the voltage is below 2.6 V, electrolyte decomposition is the main process.

4. Conclusions

In summary, we investigated the Li_2MnO_3 activation pathway and CEI formation/dissolution of $xLi_2MnO_3{\cdot}(1\text{-}x)LiNi_{0.3}Co_{0.3}Mn_{0.4}O_2$ (x = 0, 0.5, 1) cathode materials in 1 M $LiPF_6$/EC+DMC by in-situ EQCM and EIS. A synergistic effect between layered Li_2MnO_3 and $LiNi_{0.3}Co_{0.3}Mn_{0.4}O_2$ component that explains the extra-high capacity for $Li_{1.2}Ni_{0.12}Co_{0.12}Mn_{0.56}O_2$ cathode was found. The synergistic effect in Li-rich $Li_{1.2}Ni_{0.12}Co_{0.12}Mn_{0.56}O_2$ cathodes can affect the activation pathway of the Li_2MnO_3 component in Li-rich material. Specifically, the activation of pure Li_2MnO_3 is governed by chemical decomposition to Li_2O. However, Li_2MnO_3 activation in Li-rich material is dominated by electrochemical activation to O_2^{2-} (oxygen redox). Chemical decomposition does not contribute to the electrode capacity because there is no delithiation. This explains why Li-rich materials ($0.5Li_2MnO_3{\bullet}0.5LiNi_{0.3}Co_{0.3}Mn_{0.4}O_2$) have a higher capacity than the mean value of Li_2MnO_3 and $LiNi_{0.3}Co_{0.3}Mn_{0.4}O_2$.

Besides activation of Li-rich materials, it has been observed that CEI formation/dissolution accompanies Li^+ extraction/insertion. We also found that changes in the valence state of metal ions (Ni, Co, Mn) in Li-rich material can promote CEI formation. Focusing on reducing chemical

decomposition during first-cycle activation, and controlling the promotion of metal ions valence states changes should provide a route to improve the electrochemical performance of Li-rich materials.

ASSOCIATED CONTENT

Supporting Information

Impedance parameters of Li-rich $Li_{1.2}Ni_{0.12}Co_{0.12}Mn_{0.56}O_2$ at different potentials during first cycle; Optical micrograph of Li-rich material coated EQCM electrode; Refinement XRD patterns of Li-rich material; CV-EQCM test data of pure $LiPF_6$/EC+DMC electrolyte without loaded materials; Evolution of resistance ($\Delta \boldsymbol{R}$) of pure electrolyte, Li-rich, layered oxide and Li_2MnO_3 during first cycle; EIS results of Li-rich $Li_{1.2}Ni_{0.12}Co_{0.12}Mn_{0.56}O_2$ at different potentials during first cycle; EIS results of layered $LiNi_{0.3}Co_{0.3}Mn_{0.4}O_2$ during first charge.

Author Information

Corresponding Author:

* E-mail: jtli@xmu.edu.cn (J. T. Li), hmzheng@lbl.gov (H. M. Zheng), sgsun@xmu.edu.cn (S. G. Sun).

Notes:

The authors declare no competing financial interest.

Acknowledgements

This work is supported by NSFC (21621091) and Natural Science Foundation of Fujian Province of China (2015J01063). Z. W. Yin acknowledges funding support from the China Scholarship Council (201606310151). H. Zheng thanks the support of U.S. Department of Energy (DOE), Office of Science, Office of Basic Energy Sciences (BES), Materials Science and Engineering Division under Contract No. DE-AC02-05-CH11231 within the KC22ZH program.

References:

(1) Lee, J.; Urban, A.; Li, X.; Su, D.; Hautier, G.; Ceder, G. Unlocking the potential of cation-disordered oxides for rechargeable lithium batteries. *Science* **2014**, *343*, 519-522.

(2) Sathiya, M.; Abakumov, A. M.; Foix, D.; Rousse, G.; Ramesha, K.; Saubanere, M.; Doublet, M. L.; Vezin, H.; Laisa, C. P.; Prakash, A. S.; Gonbeau, D.; VanTendeloo, G.; Tarascon, J. M. Origin of voltage decay in high-capacity layered oxide electrodes. *Nature materials* **2015**, *14*, 230-238.

(3) Hy, S.; Liu, H.; Zhang, M.; Qian, D.; Hwang, B.-J.; Meng, Y. S. Performance and design considerations for lithium excess layered oxide positive electrode materials for lithium ion batteries. *Energy & Environmental Science* **2016**, *9*, 1931-1954.

(4) Zheng, J.; Gu, M.; Xiao, J.; Zuo, P.; Wang, C.; Zhang, J. G. Corrosion/fragmentation of layered composite cathode and related capacity/voltage fading during cycling process. *Nano letters* **2013**, *13*, 3824-3830.

(5) Manthiram, A.; Knight, J. C.; Myung, S. T.; Oh, S. M.; Sun, Y. K. *Advanced Energy Materials* **2016**, *6*, 1501010.

(6) Sathiya, M.; Rousse, G.; Ramesha, K.; Laisa, C. P.; Vezin, H.; Sougrati, M. T.; Doublet, M. L.; Foix, D.; Gonbeau, D.; Walker, W.; Prakash, A. S.; Ben Hassine, M.; Dupont, L.; Tarascon, J. M.

Reversible anionic redox chemistry in high-capacity layered-oxide electrodes. *Nature materials* **2013**, *12*, 827-835.

(7) Luo, K.; Roberts, M. R.; Hao, R.; Guerrini, N.; Pickup, D. M.; Liu, Y. S.; Edstrom, K.; Guo, J.; Chadwick, A. V.; Duda, L. C.; Bruce, P. G. Charge-compensation in 3d-transition-metal-oxide intercalation cathodes through the generation of localized electron holes on oxygen. *Nature chemistry* **2016**, *8*, 684-691.

(8) Seo, D. H.; Lee, J.; Urban, A.; Malik, R.; Kang, S.; Ceder, G. The structural and chemical origin of the oxygen redox activity in layered and cation-disordered Li-excess cathode materials. *Nature chemistry* **2016**, *8*, 692-697.

(9) Li, X., Qiao, Y., Guo, S., Xu, Z., Zhu, H., Zhang, X., Yuan, Y., He, P., Ishida, M. Zhou, H. Direct visualization of the reversible O^{2-}/O^{-} redox process in Li-rich cathode materials. *Advanced Materials* **2018**, *30*, 1705197.

(10) Hy, S.; Felix, F.; Rick, J.; Su, W. N.; Hwang, B. J. Direct in situ observation of Li_2O evolution on Li-rich high-capacity cathode material, $Li[Ni_xLi_{(1-2x)/3}Mn_{(2-x)/3}]O_2$ ($0 \leq x \leq 0.5$). *Journal of the American Chemical Society* **2014**, *136*, 999-1007.

(11) Jacob, C.; Jian, J.; Su, Q.; Verkhoturov, S.; Guillemette, R.; Wang, H. Electrochemical and structural effects of in situ Li_2O extraction from Li_2MnO_3 for Li-Ion batteries. *ACS applied materials & interfaces* **2015**, *7*, 2433-2438.

(12) Levi, M. D.; Salitra, G.; Levy, N.; Aurbach, D.; Maier, J. Application of a quartz-crystal microbalance to measure ionic fluxes in microporous carbons for energy storage. *Nature materials* **2009**, *8*, 872-875.

(13) Buttry, D. A.; Ward, M. D. Measurement of interfacial processes at electrode surfaces with the electrochemical quartz crystal microbalance. *Chemical Reviews* **1992**, *92*, 1355-1379.

(14) Tsai, W. Y.; Taberna, P. L.; Simon, P. Electrochemical quartz crystal microbalance (EQCM) study of ion dynamics in nanoporous carbons. *Journal of the American Chemical Society* **2014**, *136*, 8722-8728.

(15) Liu. T.; Lin. L.; Bi. X.; Tian. L.; Yang. K.; Liu. J.; Li. M.; Chen. Z.; Lu J.; Amine. K.; Xu. K.; Pan. F. In situ quantification of interphasial chemistry in Li-ion battery. *Nature Nanotechnology* **2018**, DOI: 10.1038/s41565-018-0284-y.

(16) Yin, Z. W.; Wu, Z. G.; Deng, Y. P.; Zhang, T.; Su, H.; Fang, J. C.; Xu, B. B.; Wang, J. Q.; Li, J. T.; Huang, L.; Zhou, X. D.; Sun, S. G. A Synergistic Effect in a Composite Cathode Consisting of Spinel and Layered Structures To Increase the Electrochemical Performance for Li-Ion Batteries. *The Journal of Physical Chemistry C* **2016**, *120*, 25647-25656.

(17) Arinkumar, T. A.; Wu, Y.; Manthiram, A. Factors influencing the irreversible oxygen loss and reversible capacity in layered $Li[Li_{1/3}Mn_{2/3}]O_2$-$Li[M]O_2$ (M= $Mn_{0.5-y}$ $Ni_{0.5-y}$ Co_{2y} and $Ni_{1-y}Co_y$) solid solutions. *Chemistry of Materials* **2007**, *19*, 3067-3073.

(18) Lim, J. M.; Kim, D.; Park, M. S.; Cho, M.; Cho, K. Underlying mechanisms of the synergistic role of Li_2MnO_3 and $LiNi_{1/3}Co_{1/3}Mn_{1/3}O_2$ in high-Mn, Li-rich oxides. *Physical Chemistry Chemical Physics* **2016**, *18*, 11411-11421.

(19) Armstrong, A. R.; Holzapfel, M.; Novák, P.; Johnson, C. S.; Kang, S. H.; Thackeray, M. M.; Bruce, P. G. Demonstrating oxygen loss and associated structural reorganization in the lithium battery cathode $Li[Ni_{0.2}Li_{0.2}Mn_{0.6}]O_2$. *Journal of the American Chemical Society* **2006**, *128*, 8694-8698.

(20) Wu, H. L.; Huff, L. A.; Esbenshade, J. L.; Gewirth, A. A. In Situ EQCM Study Examining Irreversible Changes the Sulfur-Carbon Cathode in Lithium–Sulfur Batteries. *ACS applied materials & interfaces* **2015**, *7*, 20820-20828.

(21) Li, Z.; Du, F.; Bie, X.; Zhang, D.; Cai, Y.; Cui, X.; Wang, C.; Chen, G.; Wei, Y. Electrochemical kinetics of the $Li[Li_{0.23}Co_{0.3}Mn_{0.47}]O_2$ cathode material studied by GITT and EIS. *The Journal of Physical Chemistry C* **2010**, *114*, 22751-22757.

(22) Xu, K. Electrolytes and interphases in Li-ion batteries and beyond. *Chemical reviews* **2014**, *114*, 11503-11618.

(23) Li, J. T.; Chen, S. R.; Fan, X. Y.; Huang, L.; Sun, S. G. Studies of the interfacial properties of an electroplated Sn thin film electrode/electrolyte using in situ MFTIRS and EQCM. *Langmuir* **2007**, *23*, 13174-13180.

(24) Edström, K.; Gustafsson, T.; Thomas, J. O. The cathode–electrolyte interface in the Li-ion battery. *Electrochimica Acta* **2014**, *50*, 397-403.

(25) Yang, Z.; Ingram, B. J.; ; Trahey, L. Interfacial studies of Li-ion battery cathodes using in situ electrochemical quartz microbalance with dissipation. *Journal of The Electrochemical Society* **2014,** *161*, A1127-A1131.

(26) Serizawa, N.; Shono, K.; Kobayashi, Y.; Miyashiro, H.; Katayama, Y.; Miura, T. Electrochemical quartz crystal microbalance measurement of a $Li_4Ti_5O_{12}$ composite electrode in a carbonate electrolyte. *Journal of Power Sources* **2015**, *295*, 162-166.

(27) Hong, J.; Lim, H. D.; Lee, M.; Kim, S. W.; Kim, H.; Oh, S. T.; Chung, G.; Kang, K. Critical role of oxygen evolved from layered Li–excess metal oxides in lithium rechargeable batteries. *Chemistry of Materials* **2012**, *24*, 2692-2697.

(28) Xiao, L.; Xiao, J.; Yu, X.; Yan, P.; Zheng, J.; Engelhard, M.; Bhattacharya, P.; Wang, C.; Yang, X.; Zhang, J. G. Effects of structural defects on the electrochemical activation of Li_2MnO_3. *Nano Energy* **2015**, *16*, 143-151.

Table and figure captions：

Table 1. The mass change and mpe values measured from the EQCM data for $Li_{1.2}Ni_{0.12}Co_{0.12}Mn_{0.56}O_2$ during first cycle. The frequency change of pure $LiPF_6$/EC+DMC (LP) electrolyte was given as comparison. The mass of loaded $Li_{1.2}Ni_{0.12}Co_{0.12}Mn_{0.56}O_2$ material is 4.258 $\boldsymbol{\mu g}$.

Table 2. The mass change and mpe values measured from the EQCM data for $LiNi_{0.3}Co_{0.3}Mn_{0.4}O_2$ during first charge. The mass of loaded $LiNi_{0.3}Co_{0.3}Mn_{0.4}O_2$ material is 4.209 $\boldsymbol{\mu g}$.

Table 3. The mass change and mpe values measured from the EQCM Data for Li_2MnO_3 during first charge. The mass of loaded Li_2MnO_3 material is 4.777 $\boldsymbol{\mu g}$.

Table 4. Comparison of mass changes of $Li_{1.2}Ni_{0.12}Co_{0.12}Mn_{0.56}O_2$ and Li_2MnO_3 materials in 4.4-4.65 V region.

Fig 1. (a) Schematic diagram of EQCM setup.

Fig 2. SEM images of: (a) Li_2MnO_3, (b) $LiNi_{0.3}Co_{0.3}Mn_{0.4}O_2$ and (c) $Li_{1.2}Ni_{0.12}Co_{0.12}Mn_{0.56}O_2$; (d) XRD patterns for the three samples; (e) Initial charge-discharge profiles at 0.1 C and (f) CV curves for the first cycle of Li_2MnO_3, $LiNi_{0.3}Co_{0.3}Mn_{0.4}O_2$ and $Li_{1.2}Ni_{0.12}Co_{0.12}Mn_{0.56}O_2$. The scan rate of CV curves is 0.2 mV s^{-1}.

Fig 3. (a) CV curve for first cycle and the simultaneous EQCM response of $Li_{1.2}Ni_{0.12}Co_{0.12}Mn_{0.56}O_2$; Plots of Δf versus ΔQ for $Li_{1.2}Ni_{0.12}Co_{0.12}Mn_{0.56}O_2$ (b) during anodic scanning and (c) cathodic scanning; (d) Plots of ΔR_{CEI} versus E (potential) for

$Li_{1.2}Ni_{0.12}Co_{0.12}Mn_{0.56}O_2$ at different potential during first charge-discharge process, and the equivalent circuit model for EIS measurements is inserted.

Fig 4. CV curve for first cycle and the simultaneous EQCM response of (a) $LiNi_{0.3}Co_{0.3}Mn_{0.4}O_2$ and (b) Li_2MnO_3; Plots of Δf versusΔQ for $Li_{1.2}Ni_{0.12}Co_{0.12}Mn_{0.56}O_2$ (c) during anodic scanning and (e) during cathodic scanning； Plots of Δf versus ΔQ for Li_2MnO_3 (d) during anodic scanning and (f) during cathodic scanning.

Scheme 1. (a) Diagram Showing the EQCM Working Principle in this Work; (b) Proposed Main Interfacial Reaction Mechanisms during First Charge and (c) The Detailed Reactions in the Li_2MnO_3 Activation Voltage Region of Li-rich oxides and Pure Li_2MnO_3; (d) Proposed Main Interfacial Reaction Mechanisms during First Discharge.

Table 1. The mass change and mpe values measured from the EQCM data for $Li_{1.2}Ni_{0.12}Co_{0.12}Mn_{0.56}O_2$ during first cycle. The frequency change of pure $LiPF_6$/EC+DMC (LP) electrolyte was given as comparison. The mass of loaded $Li_{1.2}Ni_{0.12}Co_{0.12}Mn_{0.56}O_2$ material m_1 is 4.258 $\boldsymbol{\mu g}$.

	charge					discharge			
potential region (V)	3.7-4.0	4-4.2	4.2-4.4	4.4-4.65	4.65-4.8	4.8-4.1	4.1-3	3-2.6	2.6-2
Δ*f*-pure LP (Hz)	-1.91	-1.461	-1.88	-4.51	-8.02	1.26	2.42	-0.45	-6.97
Δ*f* (Hz)	67.27	60.86	22	102.6	-6.2	29.3	-102.5	-79.65	-310.8
Δm (ng)	-90.14	-81.55	-29.48	-137.48	8.31	-39.26	137.35	106.73	416.4
$\Delta m/m_1$ (%)	-2.12	-1.92	-0.69	-3.23	0.19	-0.92	3.22	2.51	9.78
mpe ($g\ mol^{-1}$)	-32.23	-19.72	-6.03	-12.85	0.42	-1.39	25.33	34.94	53.42
ΔR	~ 0				↑	↑			

Table 2. The mass change and mpe values measured from the EQCM data for $LiNi_{0.3}Co_{0.3}Mn_{0.4}O_2$ during first charge. The mass of loaded $LiNi_{0.3}Co_{0.3}Mn_{0.4}O_2$ material m_2 is 4.209 $\boldsymbol{\mu g}$.

	Charge						Discharge				
potential region (V)	3.65 -3.9	3.9-4.1	4.1-4.4	4.4-4.53	4.53-4.65	4.65 -4.8	4.8-4.1	4.1-3.9	3.9 -3	3-2.6	2.6 -2
Δf (Hz)	42.45	134.44	132.2	44.9	19.3	21.7	6.2	-38.7	-117	-45.9	-288.7
Δm (ng)	-57.15	-180.1	-177.1	-60.2	-25.86	-29.1	-8.3	51.9	156.8	61.5	386.8
$\Delta m/m_2$ (%)	-1.36	-4.28	-4.21	-1.43	-0.61	-0.69	-0.20	1.23	3.73	1.46	9.19
mpe ($g\ mol^{-1}$)	-8.46	-56.5	-38.62	-6.73	-2.92	-1.6	-0.24	61.4	20.1	30.8	53.4
ΔR	~ 0	↑	↓	~ 0		↑	↑				

Table 3. The mass change and mpe values measured from the EQCM Data for Li_2MnO_3 during first charge. The mass of loaded Li_2MnO_3 material m_3 is 4.777 $\boldsymbol{\mu g}$.

	Charge						Discharge				
potential region (V)	OCP -3.8	3.8-4.05	4.05 -4.4	4.4-4.65	4.65-4.75	4.75 -4.8	4.8-3.9	3.9-3.3	3.3 -3	3-2.6	2.6 -2
Δf (Hz)	-29.34	3.06	-30.66	5.34	-13.94	-5.65	42.81	-6.79	-5.28	-4.18	-196.5
Δm (ng)	39.3	-4.1	41.08	-7.16	18.68	7.57	-57.36	9.1	7.07	5.6	263.27
$\Delta m/m_3$ (%)	0.82	-0.09	0.86	-0.15	0.39	0.16	-1.20	0.19	0.15	0.12	5.51
mpe ($g\ mol^{-1}$)	58.96	-8.45	21.34	-1.51	4.31	2.37	-2.69	16.74	7.55	3.34	50.12
ΔR	↑		~0	~0	↑		~0	↓	~0	↑	~0

Table 4. Comparison of mass changes and mpe value of $Li_{1.2}Ni_{0.12}Co_{0.12}Mn_{0.56}O_2$ and Li_2MnO_3 materials in 4.4-4.65 V region.

	$Li_{1.2}Ni_{0.12}Co_{0.12}Mn_{0.56}O_2$ ($0.5Li_2MnO_3 \cdot 0.5LiNi_{0.3}Co_{0.3}Mn_{0.4}O_2$)	Li_2MnO_3
Mass of loading active material (μg)	4.258	4.777
Mass ratio of Li^+	9.774%	11.882%
The maximum of mass change of Li^+ extraction (ng)	-416.164	-567.589
The maximum of mass change of Li_2MnO_3 activation (ng)	-277.442	-567.589
The real mass change In 4.4-4.65 V region (ng)	-137.484	-7.959
Mpe	-12.65	-1.51

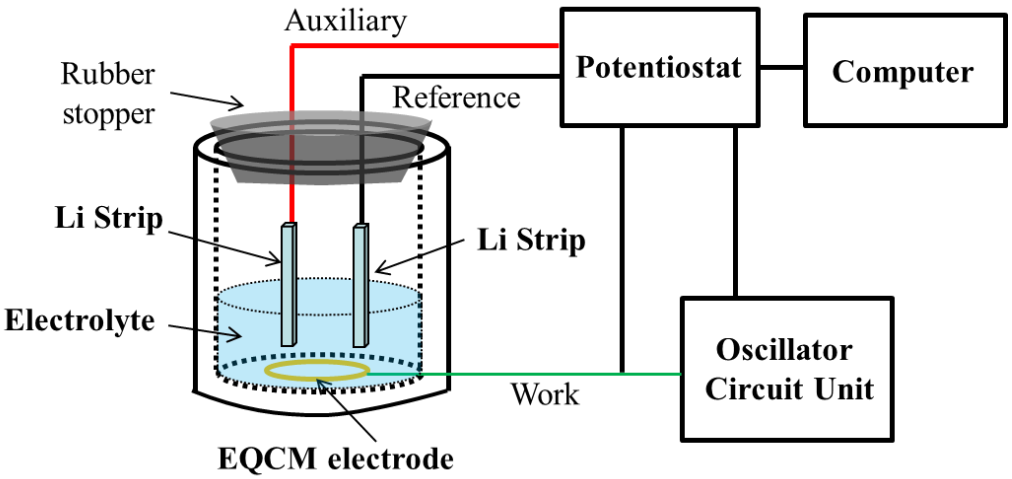

Fig 1. Schematic diagram of electrochemical quartz crystal microbalance (EQCM) experimental setup.

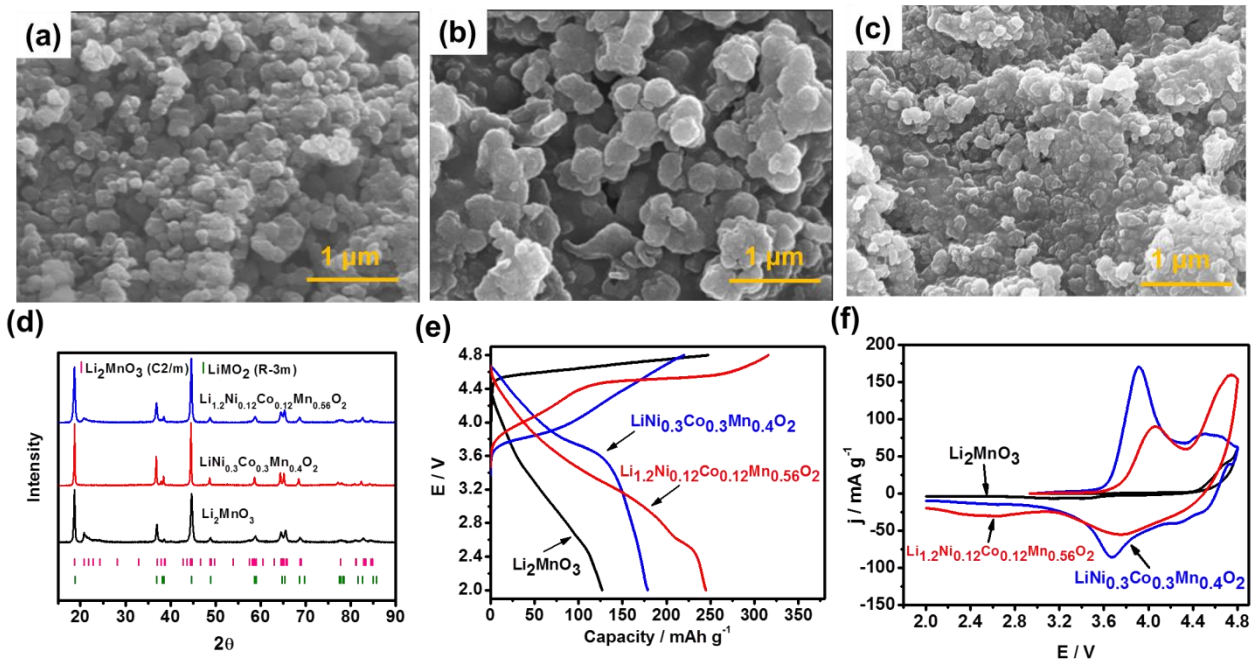

Fig 2. SEM images of: (a) Li_2MnO_3, (b) $LiNi_{0.3}Co_{0.3}Mn_{0.4}O_2$ and (c) $Li_{1.2}Ni_{0.12}Co_{0.12}Mn_{0.56}O_2$; (d) XRD patterns for the three samples; (e) Initial charge-discharge profiles at 0.1 C and (f) CV curves for the first cycle of Li_2MnO_3, $LiNi_{0.3}Co_{0.3}Mn_{0.4}O_2$ and $Li_{1.2}Ni_{0.12}Co_{0.12}Mn_{0.56}O_2$. The scan rate of CV curves is 0.2 mV s^{-1}.

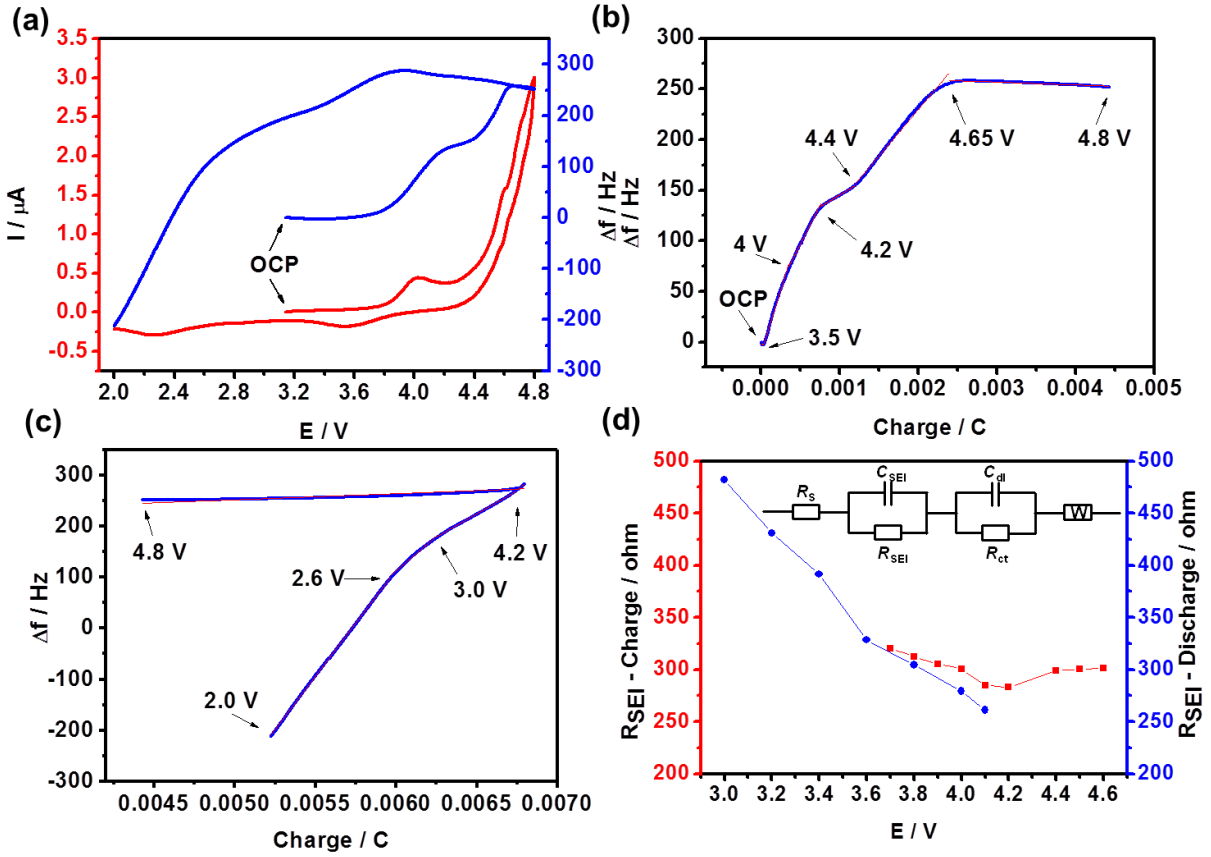

Fig 3. (a) CV curve for first cycle and the simultaneous EQCM response of $Li_{1.2}Ni_{0.12}Co_{0.12}Mn_{0.56}O_2$; Plots of Δf versus ΔQ for $Li_{1.2}Ni_{0.12}Co_{0.12}Mn_{0.56}O_2$ (b) during anodic scanning and (c) cathodic scanning; (d) Plots of ΔR_{CEI} versus E (potential) for $Li_{1.2}Ni_{0.12}Co_{0.12}Mn_{0.56}O_2$ at different potential during first charge-discharge process, and the equivalent circuit model for EIS measurements is inserted.

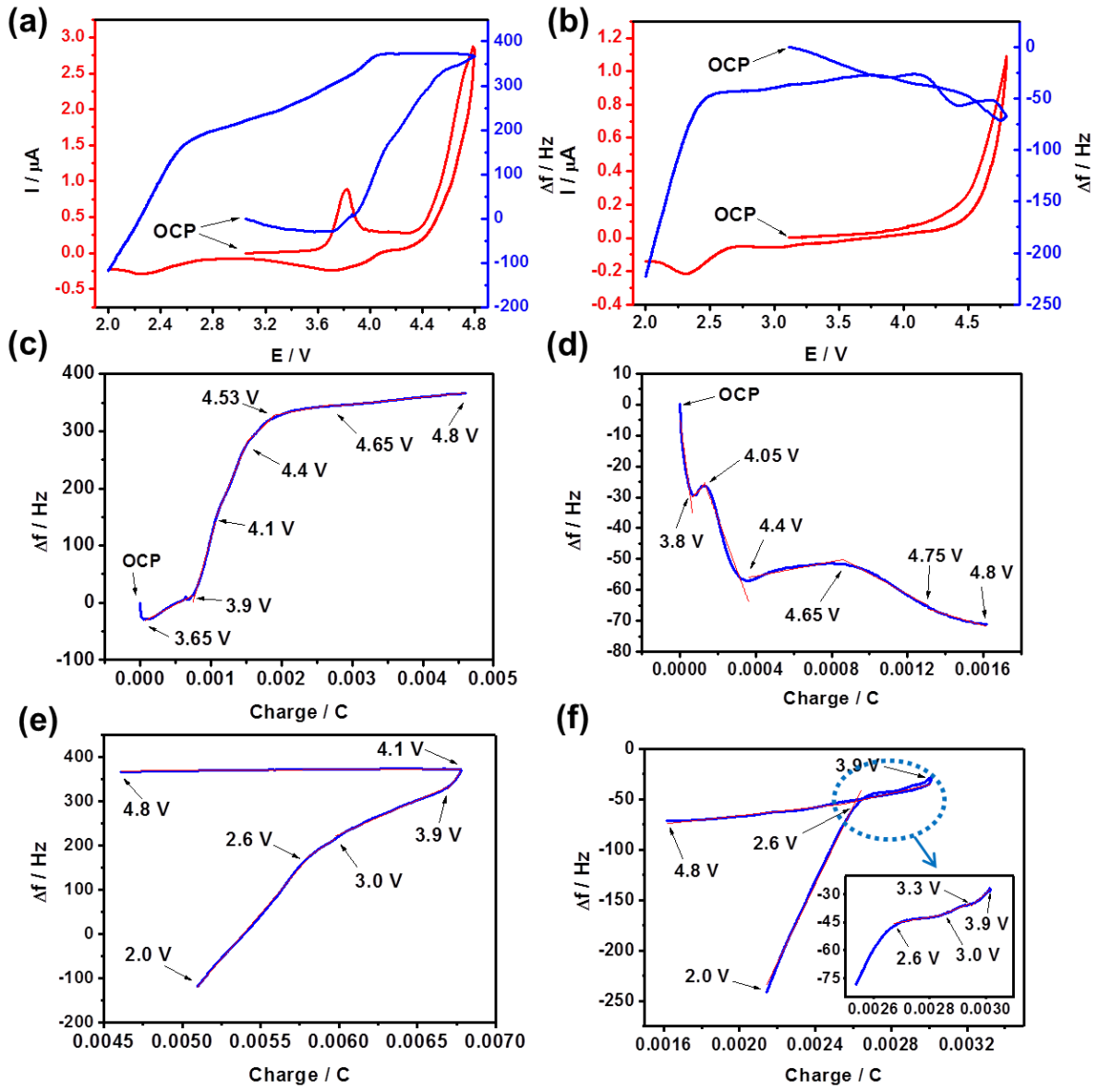

Fig 4. CV curve for first cycle and the simultaneous EQCM response of (a) $LiNi_{0.3}Co_{0.3}Mn_{0.4}O_2$ and (b) Li_2MnO_3; Plots of Δf versus ΔQ for $Li_{1.2}Ni_{0.12}Co_{0.12}Mn_{0.56}O_2$ (c) during anodic scanning and (e) during cathodic scanning；Plots of Δf versus ΔQ for Li_2MnO_3 (d) during anodic scanning and (f) during cathodic scanning.

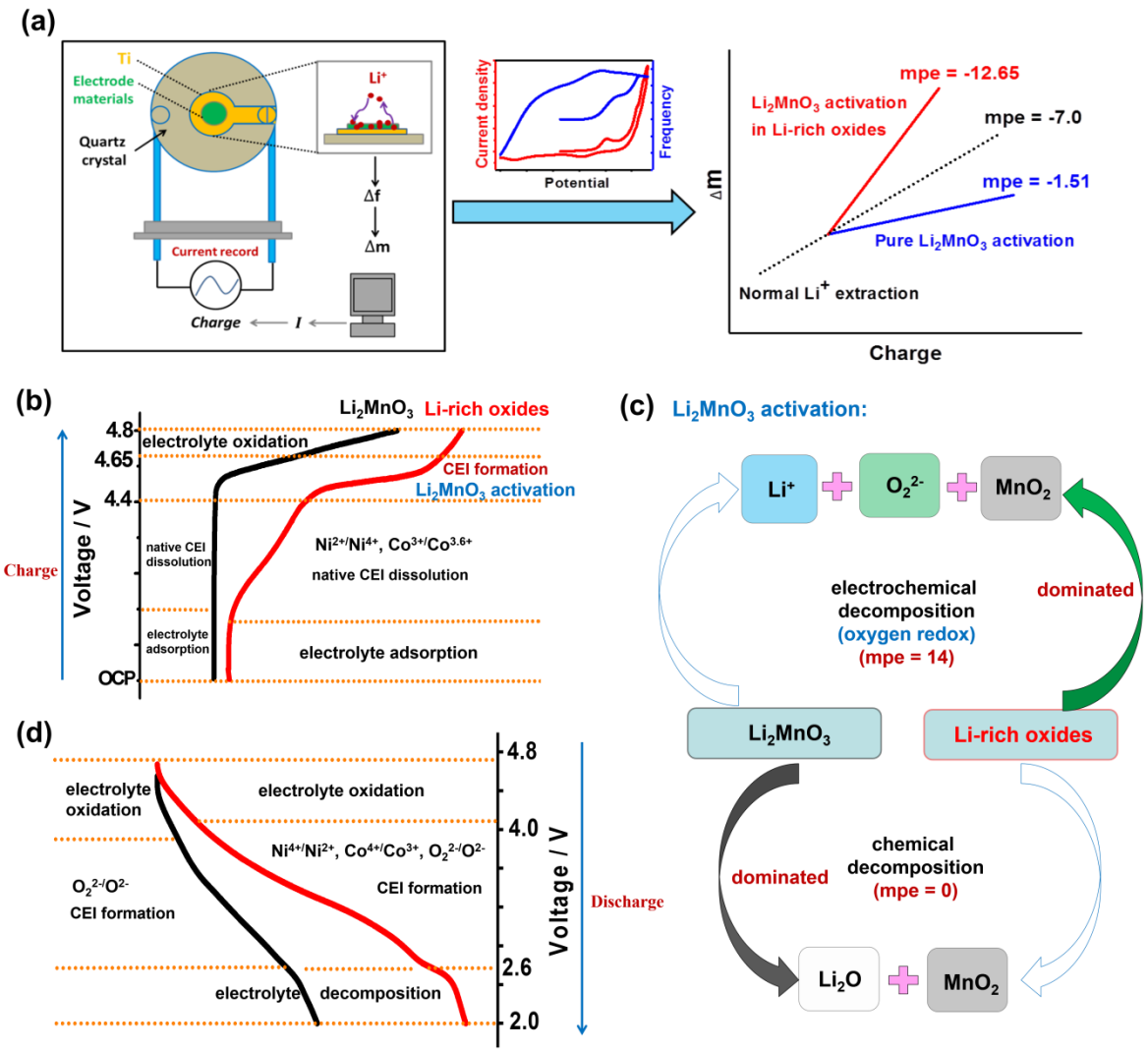

Scheme 1. (a) Diagram Showing the EQCM Working Principle in this Work; (b) Proposed Main Interfacial Reaction Mechanisms during First Charge and (c) The Detailed Reactions in the Li_2MnO_3 Activation Voltage Region of Li-rich oxides and Pure Li_2MnO_3; (d) Proposed Main Interfacial Reaction Mechanisms during First Discharge.

Table of content